ISSN 1070-3284, Russian Journal of Coordination Chemistry, 2020, Vol. 46, No. 11, pp. 729–737. © Pleiades Publishing, Ltd., 2020.
Russian Text © The Author(s), 2020, published in Koordinatsionnaya Khimiya, 2020, Vol. 46, No. 11, pp. 653–662.

EPR of Radiation-Induced Nitrogen Centers in Hydroxyapatite: New Approaches to the Study of Electron-Nuclear Interactions

F. F. Murzakhanov[a], *, G. V. Mamin[a], M. A. Goldberg[b], A. V. Knotko[c], M. R. Gafurov[a], **, and S. B. Orlinskii[a]

[a] *Kazan Federal University, Kazan, Russia*
[b] *Baikov Institute of Metallurgy and Materials Science, Russian Academy of Sciences, Moscow, 119991 Russia*
[c] *Moscow State University, Moscow, Russia*
**e-mail: murzakhanov.fadis@yandex.ru*
***e-mail: marat.gafurov@kpfu.ru*

Received April 11, 2020; revised May 16, 2020; accepted May 19, 2020

Abstract—Radiation-induced impurity nitrogen centers (NO_3^{2-}) in nanosized powders of synthetic hydroxyapatite are studied by pulse EPR and pulse double-frequency EPR, which is named the NMR detected by electron–electron double resonance (ELDOR detected NMR, EDNMR) method. The EPR signals caused by the interaction of the electron of NO_3^{2-} with the environmental nuclei (^1H, ^{14}N, and ^{31}P) are identified, and the parameters of the hyperfine and quadrupole interactions of the electron with the ^{14}N nuclei are determined. The possibility of using the EDNMR method in the X-band of microwave frequencies ($\nu_{mw} \approx 9$ GHz) at room temperature to obtain a detailed information about peculiarities of electron-nuclear interactions in hydroxyapatite is demonstrated.

Keywords: EPR, EDNMR, hydroxyapatite, nitrogen centers, electron-nuclear interactions
DOI: 10.1134/S1070328420110044

INTRODUCTION

The materials based on calcium phosphates (CaP) of the biogenic and synthetic origin evoke newly increasing interest in the recent decades, since the tissue engineering technologies are being developed and CaP are propagated in biological objects [1–3]. A series of pathologies (tumor, cardiovascular, and other diseases) with diverse manifestations can be related to the formation of organomineral deposits in various organs and tissues of the human organism [4]. Calcium phosphate, which is assigned, to certain approximation, to hydroxyapatite (HAp) with the chemical formula $Ca_{10}(PO_4)_6(OH)_2$, is weakly crystallized, as a rule, and is nonstoichiometric because of significant amounts of foreign ions, is the main inorganic phase of the pathogenic calcification of collagen, muscular, bone, and tooth tissues [5–8]. Some of the ions are located in the crystal lattice of apatite, and other are only adsorbed on the apatite surface [9].

The evolution of technologies in the field of tissue engineering is associated with the design of materials of several generations: from bioinert to osteoinductive (stimulating osteosynthesis) materials [10, 11]. Along with biomedical applications, modified synthetic HAp can be used as highly efficient absorbents of nitrates from soil and subterranean waters [12], as supports for catalysts [13], and others. The selective anticancer activity of HAp nanocrystals was demonstrated [14, 15].

In spite of numerous studies performed, many important problems related to anionic and cationic substitutions in HAp remain insufficiently studied and the data of many works are contradictory. The most contradictory information is associated with the possibility of nanoparticle doping, forms of incorporation and localization sites of impurities in biominerals and synthetic samples, and the problem of choosing an appropriate analytical method for the detection of impurity structures.

The centers formed under ionizing irradiation are often used as paramagnetic probes for the EPR study of natural and synthetic HAp. The methods of EPR and electron-nuclear double resonance made it possible to identify a considerable amount of inorganic radicals in the irradiated samples: O_3^-, CO_3^-, CO_3^{3-}, CO_2^-, CO, PO_4^-, and H^0 [16]. The nature of radiative EPR signals in other CaP remains poorly studied [2, 9, 17].

The development of the EPR techniques using various calculation procedures makes it possible to discover new aspects of applying signaling paramagnetic

probes. It was shown by the EPR research group at the Kazan Federal University that a change in the spectral characteristics of the EPR signals from carbonate radicals in the organomineral deposits can be used for the characterization of the degree of calcinification of vessel walls in the case of atherosclerosis [18]. The Mn^{2+} manganese ions, whose relaxation characteristics (transverse electron relaxation time) correlates with the stability of atherosclerotic plaques, were found in atherosclerotic plaques using a high sensitivity of EPR methods in high magnetic fields [19]. The carbonification of the synthesized nano- and microparticles of HAp was found to decrease the amount of nitrogen-containing impurities incorporated into the HAp structure during the popular synthesis of the samples from solutions of NH_4OH and HNO_3 [20].

Nitrogen-containing radicals are of special significance among a wide series of paramagnetic centers playing a significant (active and signaling) role in the vital activity of living organisms and metabolism processes and having a broad area of practical and potential applications [21]. Stable nitroxyl radicals and spin traps based on them have efficiently been used as paramagnetic probes for the study of diverse molecular systems in the liquid and solid states since the 1960s [22, 23]. Nitroxyl radicals are irreplaceable as spin labels in the study of structures of various biomolecules by electron–electron double resonance (ELDOR) methods [24–27]. However, although nitrogen-containing centers have been studied for a long time, many details of their structure, dynamics, properties, and participation in metabolic processes remain poorly studied. Nitrates (NO_3^-) and nitrites (NO_2^-) have been studied up to recently only either as inert final products of NO nitrogen oxide metabolism, or toxic and carcinogenic components that get into the organism via the food chain. Fairly convincing evidences have been accumulated within recent decades that these anions in the blood and tissues of living organisms should be considered as pools necessary for nitrogen storage; that is, nitrates and nitrites are actively involved in the transformation cycle of nitrogen and its compounds in living organisms via the mechanism complementary to that acknowledged in animal and plant physiology and using NO synthase [28]. The studies prove that the interaction of inorganic nitrate (NO_3^-) exerts an anti-inflammatory effect and leads to the stabilization of atherosclerotic plaques, whereas the influence of nitrites is not pronounced [29]. The nitrogen radical NO_3 discovered more than 130 years ago is important for the troposphere chemistry and is a classical example for the "failure" of the Born–Oppenheimer approximation for the description of this radical. The absorption spectrum, electronic structure, and photochemical properties of this radical remain rather unclear and enforce researchers to use more and more subtle theoretical and experimental methods for its investigation [30, 31]. Unexpectedly high experimental coefficients of ^1H NMR signal enhancement due to the dynamic nuclear polarization effect in aqueous solutions of nitroxyl radicals in strong magnetic fields [32] and the discovery of the dynamic nuclear polarization effect using the nitrogen-coordinated vanadium porphyrin complexes in the petroleum systems [33] prompted researchers to revise the accepted calculation models for the dynamic characteristics of nitrogen-containing centers in aqueous and oil-dispersion media. A number of works including the studies of the EPR group of Professor Vladimir Minin was devoted to the identification and new aspects of the EPR studies of various nitrogen centers in diamonds and nanodiamonds [34, 35].

We showed in our previous publications that the radiation-induced nitrate radical NO_3^{2-} can be used as an efficient spin probe for studying the structure and chemical composition during the modification of powdered micro- and nanosamples of HAp and other CaP by various anions and cations (e.g., CO_3^{2-} [22], Mn^{2+} [36, 37], Pb^{2+} [38], and Al^{3+} [39] ions) using the EPR and ELDOR methods. The spectroscopic and relaxation characteristics of NO_3^{2-} vary upon HAp codoping and a decrease in the particle size. Using a combination of the multifrequency stationary and pulse EPR and ELDOR methods on ^1H and ^{31}P nuclei and calculations in terms of the density functional theory, we determined the structure and localization of the radiation-induced NO_3^{2-} radical in the HAp samples. It is shown that the hyperfine interaction of the electron in the stable NO_3^{2-} radical with its nitrogen nucleus can be used for the identification of nitrate ion dislocations in the crystal lattice [40].

The results of studying the radiation-induced nitrogen centers NO_3^{2-} in synthetic HAp powders by the ELDOR detected NMR method (EDNMR) at room temperature in the 3-cm X-band are presented in this work. As far as we know, EDNMR was not applied earlier for the study of similar systems. Moreover, in the majority of the known applications pulse the EDNMR method is used at higher frequencies and at low temperatures for a higher spectral resolution and the possibility to observe the pulse EPR signal [41–43]. Since pulse EDNMR is not a standard EPR procedure of physicochemical analysis of substances, a part of the study is a brief theoretical introduction into the essence of the EDNMR technique necessary for understanding the results obtained.

EXPERIMENTAL

Synthesis of HAp was carried out by the precipitation method from aqueous solutions: a solution of ammonium phosphate and ammonia were introduced into a solution of calcium nitrate. The precipitation

was carried out at pH 11.5 ± 0.5. The amounts of the components were calculated according to reaction (1)

$$10Ca(NO_3)_2 + 6(NH_4)_2HPO_4 + 8NH_4OH = Ca_{10}(PO_4)_6(OH)_2 + 20NH_4NO_3 + 6H_2O. \quad (1)$$

The formed precipitate was subjected to aging for 21 days to increase the degree of crystallization of the apatite phase, filtered, and dried at 60°C.

The prepared materials were studied by X-ray diffraction analysis (XRD) (Rigaku D/max-2500), IR spectroscopy (Nikolet Avatar), and scanning electron microscopy (SEM) (CrossBeam 1540 EsB, Carl Zeiss) for the determination of the morphology and particle size. According to the XRD data, the powder is single-phase, and the peaks correspond to HAp (PDF file #09-0432) with the space group $P6_3/m$. The data of IR spectroscopy confirm the formation of the apatite structure. The IR spectra (ν) exhibit absorption bands of OH groups ($\nu(OH^-)$) at 3575 and 630 cm^{-1} and of phosphate groups as follows: a doublet $\nu_4(PO_4^{3-})$ at 570 and 610 cm^{-1}, a broad triplet $\nu_2(PO_4^{3-})$ at 420–480 cm^{-1}, peaks $\nu_1(PO_4^{3-})$ at 962 cm^{-1} and $\nu(PO_4^{3-})$ at 875 cm^{-1}, and a doublet $\nu_3(PO_4^{3-})$ at 1095 and 1040 cm^{-1}. The nitrate groups are presented by high-intensity absorption bands $\nu(NO_3^-)$ at 830 cm^{-1} and a doublet at 1395 and 1370 cm^{-1} assigned to the retention of traces of NH_4NO_3 as a by-product of the synthesis and to NO_3^- adsorption on the HAp surface. на The SEM study showed that the materials were formed by particles of the round and oval morphology 10–20 nm in size forming dense agglomerates.

EPR experiments were carried out on an Elexsys E580 spectrometer (Bruker) in the X-band (ν_{mw} = 9.6 GHz) at room temperature (T = 297 K). The measurements were performed in the pulse mode [44]. The EPR spectra were recorded using the detection of the integral intensity of electron spin echo (ESE) depending on the magnetic field intensity B_0. The Hahn echo sequence π/2–τ–π–τ–ESE was used, where the delay between the pulses was τ = 200 ns and the π/2 pulse duration was 16 ns. The Hahn sequence was also used to determine the spin–spin relaxation time (T_2). In this case, the ESE integral intensity was measured at fixed B_0 depending on τ, which increased to a necessary value with an increment of 4 ns. The spin-lattice relaxation time (T_1) was determined by the "inversion–recovery" sequence $\pi-T_{delay}-\pi/2-\tau-\pi-\tau-$ESE. When measuring T_1, the ESE integral intensity was measured at fixed B_0 depending on the time T_{delay}, which was varied from 1.5 μs (with an increment of 256 ns) to the moment of the complete recovery of the initial amplitude of the ESE signal.

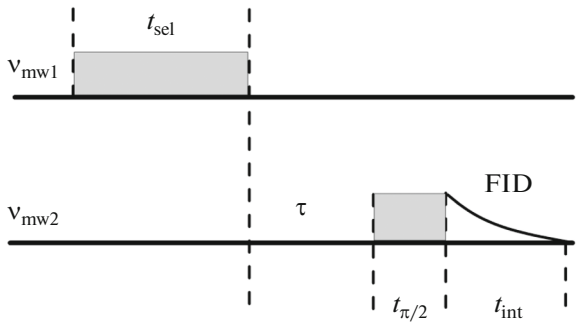

Fig. 1. Scheme of the pulse sequence used in the EDNMR method [46].

To generate stable paramagnetic centers, which were absent in the nominally pure material, the X-ray irradiation of the sample was used on an URS-55 setup (U = 55 kV, I = 18 mA, tungsten anticathode) at room temperature for 1 h with a calculated irradiation dose of 30 kGy. The EPR spectra were simulated using the Matlab package of applied programs with the additional Easyspin module [45].

The EDNMR method was accomplished on an Elexsys E580 EPR spectrometer (Bruker) in the X-band (ν_{mw1} or ν_{obs} = 9.59 GHz, $B_0 \approx 0.34$ T) at T = 297 K. An E580-400U pulse ELDOR module and an ER 4118X-MD5 dielectric circular resonator were used to perform electron–electron double transitions forming the basis of the EDNMR method. An E580-400U module is necessary for the generation and broach of the second independent microwave frequency (ν_{mw2} or ν_{pump}) in the range from 9.3 to 10 GHz. Owing to the controlled quality factor, an ER 4118X-MD5 resonator makes it possible to optimize the bandwidth of resonance frequencies according to specific experimental requirements.

To achieve a high resolution ability, the duration of the selective pulse (t_{sel}) was chosen to be equal to 6 μs, which corresponds to the excitation band in the EPR spectrum with ΔB = 0.47 G. The detecting pulse duration ($t_{\pi/2}$) is 300 ns at the detection of the free induction decay (FID) (Fig. 1).

The following detection parameters were chosen to increase the sensitivity and minimize the possibility of the appearance of various artifacts: integration time t_{int} = 250 ns and interval between pulses τ = 3 μs (quality factor of the resonator Q = 200 at the frequency ν = 9.59 GHz, dead time ≈200 ns).

EDNMR for S = 1/2 and I = 1/2. Let us consider the hyperfine interaction (HFI) in the system consisting of the electron (S = 1/2) and magnetic nucleus (I = 1/2). This configuration is characterized by the four-level system: 1 = |β, α⟩, 2 = |β, β⟩, 3 = |α, α⟩, 4 = |α, β⟩, where the first index in braces is the projection of the electron spin, and the second index in the projection of the nuclear spin (Fig. 2).

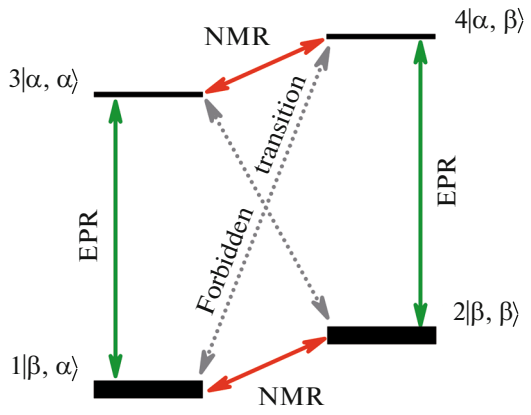

Fig. 2. Scheme of the levels for the spin system with $S = 1/2$ and $I = 1/2$ and hyperfine interaction [46].

This spin system is described by the following Hamiltonian:

$$\hat{H} = \omega_s \hat{S}_z + \omega_I \hat{I}_z + A\hat{S}_z\hat{I}_z + B\hat{S}_z\hat{I}_x, \qquad (2)$$

where the first two terms are the electron and nuclear Zeeman interactions, and the remaining two terms are the components of the axial HFI. The values of A and B are related to the values of HFI in the canonical positions $A_\parallel = A_{zz}$ and $A_\perp = A_{xx} = A_{yy}$ via the corresponding equations: $A = A_\parallel\cos^2\theta + A_\perp\sin^2\theta$, $B = (A_\parallel - A_\perp)\sin\theta\cos\theta$, where θ is the angle between the crystalline axis c and magnetic field B_0.

Three types of transitions are marked in Fig. 2: (i) allowed EPR transitions $1 \to 3$ and $2 \to 4$ with the frequencies ν_{13} and ν_{24}, respectively (as a rule, the probability of these transitions is high, and the selection rule is $\Delta M_s = \pm 1$, $\Delta M_I = 0$); (ii) forbidden EPR transitions ($\Delta M_s = \pm 1$, $\Delta M_I = \pm 1, \pm 2$) $1 \to 4$ and $2 \to 3$ with the frequencies ν_{14} and ν_{23}, respectively (as a rule, the probability of these transitions is low); and (iii) allowed NMR transitions ($\Delta M_s = 0$, $\Delta M_I = \pm 1$) $1 \to 2$ and $3 \to 4$ with the frequencies ν_{12} and ν_{34}, respectively (the probability of these transitions is high under the corresponding radio-frequency treatment).

An EDNMR experiment is the electron polarization transfer between the allowed levels 1–3 or 2–4 to the levels corresponding to the allowed NMR transitions 1–2 or 3–4, thus changing the absorption intensity of the EPR signal. The first selective pulse with a variable frequency is necessary for the excitation of forbidden transitions with the turn of the spin magnetization by the angle π. The second detecting pulse at a fixed frequency (observation frequency) is necessary for the excitation of allowed EPR transitions with the corresponding turning angle of the spin magnetization by $\pi/2$. The durations of the selective and detecting pulses differ significantly, which is due to a substantial difference between the probabilities of the forbidden (I_f) and allowed (I_a) transitions. The optimum turning angle by the selective pulse is determined as follows:

$$\beta_f = \omega_I t_{sel} (I_f)^{1/2} = \beta_0 (I_f)^{1/2}, \qquad (3)$$

where $\omega_I/2\pi = g_e\mu_e B_1/h$, and $\beta_0 = \omega_I t_{sel}$ is the turning angle for $I_f = 1$.

The selective pulse is tens and even hundreds μs because of the dependence of the magnetization turning angle on the probability of transition. The duration of the detecting pulse rarely reaches 1 μs, since $I_a \gg I_f$. The selective pulse inducing transitions between the forbidden transitions 1–4 or 2–3 changes the population of these levels and in parallel equalizes the polarization between the levels 1–3 and 2–4.

Detection is usually carried out at the microwave frequency for one of the allowed EPR transitions, whereas the selective pulse frequency varies in a wide range. Thus, the EDNMR spectrum is the dependence of the integral intensity of the allowed EPR transition on the selective pulse frequency. The EPR signal of the allowed transition decreases when the selective pulse frequency coincides with the frequency of one of the forbidden transitions.

The dip in the EDNMR spectrum depends on the probability of the allowed and forbidden transitions, which are determined as follows:

$$I_f = \sin^2\eta, \qquad (4a)$$

$$I_a = \cos^2\eta, \qquad (4b)$$

where $\eta = (1/2)(\eta_\alpha - \eta_\beta)$, $\eta_\alpha = \arctan[-B/(A + 2\omega_I)]$, $\eta_\beta = \arctan[-B/(A - 2\omega_I)]$.

The dip depth coefficient is written as

$$h = 1 - I_a\cos\left(\beta_0 (I_f)^{1/2}\right) - I_f\cos\left(\beta_0 (I_a)^{1/2}\right). \qquad (5)$$

Equation (5) allows one to conclude the following: (i) the higher the degree of axial anisotropy of the HFI, the higher the probability of the forbidden transitions and, hence, the EDNMR effect would be more pronounced; (ii) when the HFI value is comparable with or almost equal to the Larmor frequency of the nucleus, then the probability of the forbidden transition would be as high as that of the allowed EPR transition; and (iii) in the canonical orientations at $\theta = 0°$ and $\theta = 90°$, $\eta = 0$ thus vanishing the probability of the forbidden transition.

Equation (5) takes into account the fact that both allowed and forbidden transitions can be overlapped by the selective or detecting pulse at the nonuniform EPR linewidth for the frequency excitation of the spin package. The term proportional to $\cos(\beta_0(I_f)^{1/2})$ corresponds to the forbidden transition, which is resonance to the selective pulse frequency. Since the detecting pulse is supplied at the allowed transition frequency, its intensity is taken into account using the multiplication by I_a. The term proportional to $\cos(\beta_0(I_a)^{1/2})$ represents the case where the allowed transition is in res-

onance to the selective pulse frequency. In this case, the observed transition is forbidden, which is taken into account by the factor I_f [46, 47].

EDNMR of nitrogen radicals ($S = 1/2$ and $I = 1$). The system of the radiation-induced nitrate radical NO_3^{2-} (as that of the nitroxyl radical) is described using the quantum numbers $S = 1/2$ and $I = 1$ (for nuclei ^{14}N). As compared to Eq. (2), the spin-Hamiltonian is supplemented by the quadrupole interaction

$$\hat{H} = g_e\beta_e B_0\hat{S} - g_n\beta_n B_0\hat{I} + \hat{S}A\hat{I} + \hat{I}P\hat{I}, \qquad (6)$$

where g_e and g_n are the electron and nuclear spectroscopic splitting tensors, respectively; β_e and β_n are the electron and nuclear magnetons, respectively; and A and P are the hyperfine and quadrupole interaction tensors, respectively. The energy levels of the considered spin system assuming that $A > 2\nu_I$ (ν_I is the Larmor frequency of the nitrogen nucleus in the fixed field intensity B_0) are presented in Fig. 3. Four more forbidden transitions, whose probability can differ from zero due to level mixing, are related to each of three allowed EPR transitions.

In the first order of the perturbation theory with allowance for $A > 2\nu_I$ for the EDNMR transitions, we have

$$\nu^{\alpha}_{sq1} = A/2 - \nu_I - 3P/2, \qquad (7a)$$

$$\nu^{\alpha}_{sq2} = A/2 - \nu_I + 3P/2, \qquad (7b)$$

$$\nu^{\alpha}_{dq} = A - 2\nu_I, \qquad (7c)$$

$$\nu^{\beta}_{sq1} = A/2 + \nu_I - 3P/2, \qquad (7d)$$

$$\nu^{\beta}_{sq2} = A/2 + \nu_I + 3P/2, \qquad (7e)$$

$$\nu^{\beta}_{dq} = A + 2\nu_I, \qquad (7f)$$

where indices sq and dq designate single-quantum and double-quantum transitions, respectively.

Whence, using these equations and experimental values for the transitions in the EDNMR frequency spectra, one can directly determine the quadrupole splitting accurate within sign [48, 49]

$$\nu^{\beta}_{sq1} - \nu^{\alpha}_{sq2} = 2\nu_I - 3P, \qquad (8a)$$

$$\nu^{\beta}_{sq2} - \nu^{\alpha}_{sq1} = 2\nu_I + 3P. \qquad (8b)$$

RESULTS AND DISCUSSION

The pulse EPR spectrum of the powdered HAp sample after X-ray irradiation is shown in Fig. 4. The signal is caused by the presence in the sample of the radiation-induced nitrate radical NO_3^{2-} of the axial symmetry described by the spin-Hamiltonian [40] in the following form:

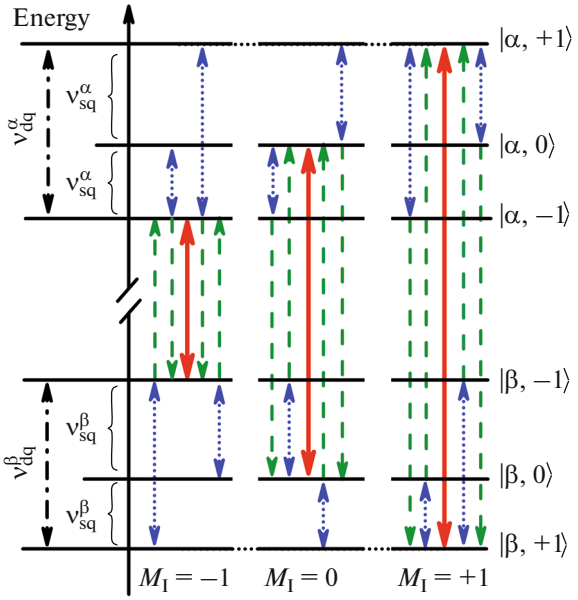

Fig. 3. Scheme of the energy level splitting in the magnetic field for the spin system with $S = 1/2$ and $I = 1$. The case for $A > 2\nu_I$. Solid lines (red) indicate allowed EPR transitions, dashed lines (green) indicate forbidden EPR transitions, and dotted lines (blue) are NMR transitions [46]).

$$\hat{H} = g_{\parallel}\beta B_z\hat{S}_z + g_{\perp}\beta\left(B_x\hat{S}_x + B_y\hat{S}_y\right) + A_{\parallel}\hat{S}_z\hat{I}_z + A_{\perp}\left(\hat{S}_x\hat{I}_x + \hat{S}_y\hat{I}_y\right). \qquad (9)$$

The EPR spectral parameters for the nitrogen radical in HAp are the following:

$g_{\parallel}$	$g_{\perp}$	$A_{\parallel}$	$A_{\perp}$
2.002	2.006	66.8 G (187 MHz)	34 G (95.2 MHz)

The pronounced anisotropy of the g and A tensors for various orientations of the external magnetic field in the powder spectrum allows the spectral resolution to perform for the nanocrystal orientations from parallel ($c \parallel B_0$) to perpendicular ($c \perp B_0$).

Since the relaxation characteristics play one of the key roles for the successful EDNMR experiment (long-range pulse sequences and long pulses are used in the method), the times T_1 and T_2 were measured on all components of the EPR spectrum presented in Fig. 4 (corresponding to the transitions with $M_I = 0$ and ± 1). As it turned out, for all transitions $T_2 = 3 \pm 0.3$ μs, which made it possible to detect the EDNMR signal at room temperature. The relatively short longitudinal relaxation time $T_1 = 30 \pm 1.2$ μs allows one to establish the repetition value of pulse sequences $T_{rep} = 5T_1 \approx 150$ μs for the possibility of signal acquisition and increasing the signal to noise ratio within rather short experimental time.

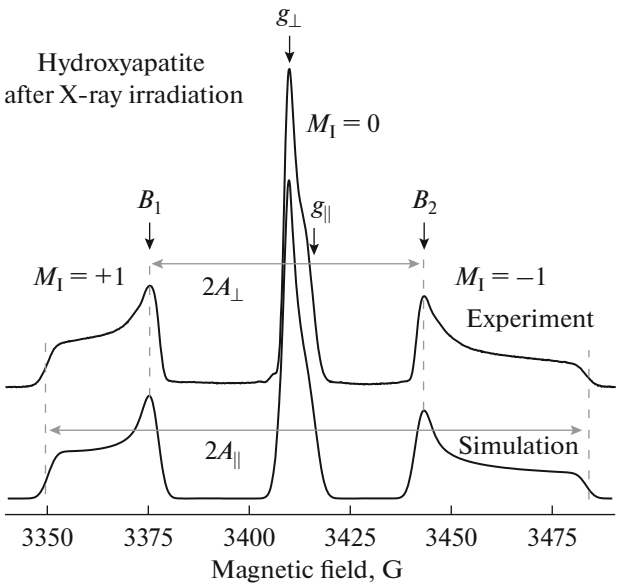

Fig. 4. EPR spectrum of the nitrogen radical in the HAp matrix obtained by the detection of the ESE integral intensity at various B_0. The bottom curve is the simulation of the experimental spectrum.

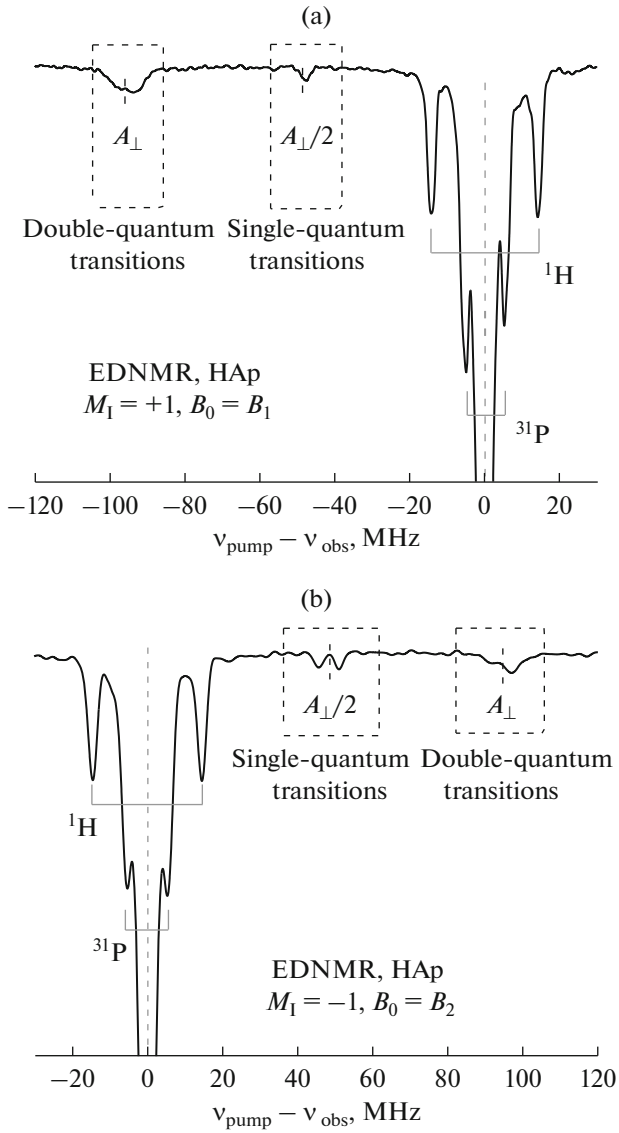

Fig. 5. Overall EDNMR spectrum for two different HFS transitions with M_I = (a) +1 and (b) −1 in the magnetic fields B_1 and B_2, respectively (see Fig. 4).

The shape of an EDNMR spectrum depends on the quantum number M_I. In our measurements, the values of B_0 were fixed on the perpendicular orientation of the hyperfine structure (HFS) designated by arrows in Fig. 4 as B_1 and B_2 to increase the signal to noise ratio separately for each HFS transition with M_I equal to +1 and −1, respectively.

The overall spectra presented in Fig. 5 represent the signals at ±6 and ±14.8 MHz corresponding to the Larmor frequencies of phosphorus ^{31}P ($I = 1/2$) and hydrogen ^{1}H ($I = 1/2$) at $B_0 \approx 0.34$ T. These signals should be expected, since hydrogen and phosphorus are structural units of HAp and indicate that the studied nitrogen impurities are inserted into the crystal lattice of HAp. The absence of additional structures or subsplittings for these nuclei indicates an insufficient resolution of the EDNMR method at least at room temperature in the X-band . The HFI of the nitrogen radical with the ^{31}P and ^{1}H nuclei in HAp studied by the ELDOR methods (the corresponding spectra were recorded at $T < 100$ K) were described in detail [40].

The signals observed at the frequencies $\nu = \pm 47.5$ and ±95 MHz are of most interest. It follows from the calculations presented above for various electron–electron transitions (7a)–(7f) and the known HFI constants (see above) that these transitions are due to the anisotropic hyperfine interaction of the lone electron with the nitrogen nucleus for which the HFI value A exceeds the Larmor frequency of ^{14}N nuclei ($\nu_{Larmor} = 1.04$ MHz for $B_0 \approx 0.34$ T). This results in the localization of the signal in the ranges of the halved (for the single-quantum transitions with $\Delta M_I = \pm 1$) and integer quantity of the HFI (for the double-quantum transitions with $\Delta M_I = \pm 2$).

An additional splitting (Fig. 6) is observed by the detailed examination of the spectrum in the range $\Delta\nu > 0$ ($M_I = -1$) for the single-quantum transition.

The centers of the lines presented in Fig. 6 coincide to high accuracy with $A_\perp/2$ determined from the EPR spectrum. On the basis of Eqs. (7a), (7b), (7d), and (7e) for the single-quantum transitions, we may conclude that the observed splitting appears due to the quadrupole moment in the ^{14}N nuclei. Assuming that the A and P tensors in Eq. (6) are collinear, the value (and sign) of the quadrupole splitting can be calcu-

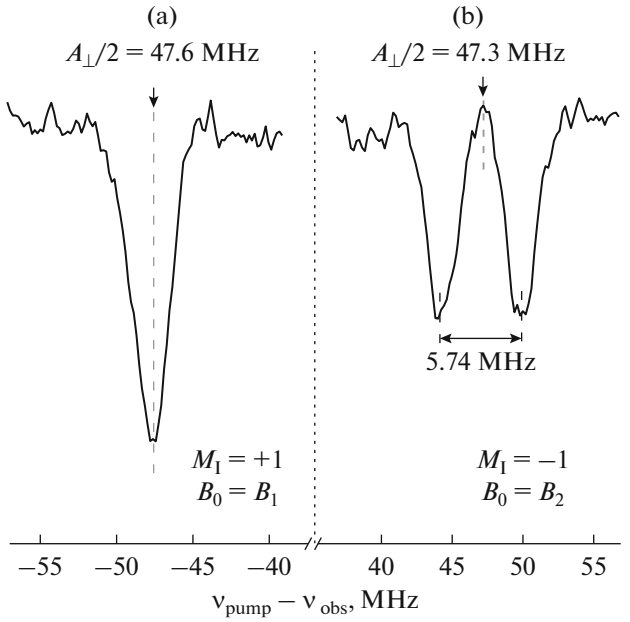

Fig. 6. EDNMR spectra for the single-quantum transitions presented in Fig. 5 with (a) $M_I = +1$ and (b) $M_I = -1$.

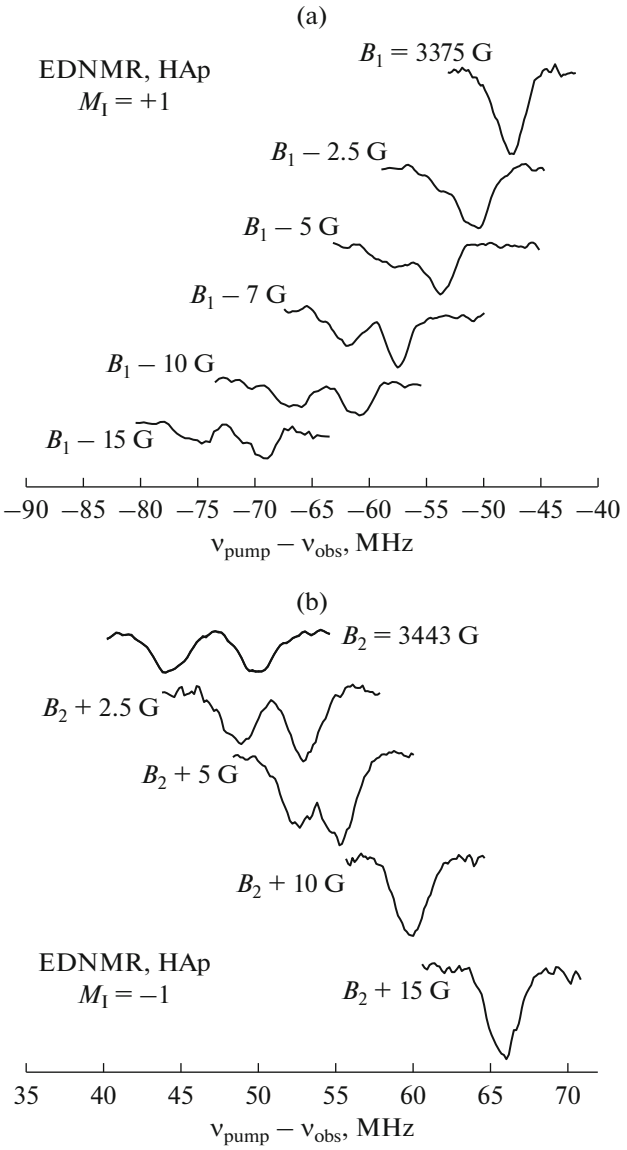

Fig. 7. EDNMR spectra for the single-quantum transitions with a change in B_0 from (a) the initial B_1 for $M_I = +1$ and (b) B_2 for $M_I = -1$ corresponding to the rigidly perpendicular orientation ($A_\perp$) in the direction of the parallel orientation ($A_\parallel$).

lated rather easily. Using Eq. (8b), we have that $P_\perp$ = 1.2 MHz. The Larmor frequency of nitrogen at $B_0 \approx$ 0.34 T is comparable with the quadrupole splitting. Therefore, additional splittings are absent for the HFS line with $M_I = +1$ due to mutual compensation.

One of the proofs of the fact that the line splitting for the single-quantum transition is actually induced by the quadrupole interaction is the angular dependence for P

$$P(\theta) = P\left(3\cos^2\theta - 1\right). \quad (10)$$

The anisotropic EPR spectrum and a fairly narrow excitation spectrum make it possible to measure the "angular dependence" of the quadrupole splitting. According to the orientation dependence of the HFI constant A, as can be seen from Fig. 7, the splitting changes appreciably (Table 1) thus confirming the advanced assumption.

Probably, anisotropy of A and P is a reason for the EDNMR spectrum broadening for the central transition of the HFS with $M_I = 0$ containing signals from all orientations of HAp nanocrystals, which makes the spectrum poorly informative. The detailed calculated model and interpretation of the angular dependence of P requires further studies, since the data from Table 1 assume that the tensors A and P are noncollinear as in the case of petroporphyrins [50].

Thus, the pulse EPR and EDNMR study of the radiation-induced impurity nitrogen centers NO_3^{2-} in powders of synthetic HAp allowed us to determine the parameters of hyperfine and quadrupole (for the first time) interaction of the electron with the ^{14}N nuclei: $A_\parallel = 187$ MHz, $A_\perp = 95$ MHz, and $P = 1.2$ MHz. The possibility of observation of the resolved EDNMR spectra is due to a good localization of the nitrogen center (in the phosphate position, see [38]) and the absence of g, A, and electric field gradient scattering. The prolonged time of phase coherence ($T_2 \approx 3$ μs) makes it possible to increase the pulse duration for the excitation of spin packages in a narrower frequency range. The orientation-selective measurements were carried out in the X-band due to the A-tensor anisotropy. These factors favor the observation of EDNMR spectra in a precisely specified (chosen) orientation

Table 1. Splitting values in the EDNMR spectra of the single-quantum transitions at various B_0

Fixed magnetic fields vs. B_0	Splitting of single-quantum transition $\lvert\nu_{sq2} - \nu_{sq1}\rvert$, MHz	
	$B_1 - {}_{\Delta}B$; $\Delta\nu < 0$ ($M_I = +1$)	$B_2 + {}_{\Delta}B$; $\Delta\nu > 0$ ($M_I = -1$)
$B_0 = B_{1,2}$	0	5.7
$B_0 = B_{1,2} \pm 2.5$ G	~0.5	4.1
$B_0 = B_{1,2} \pm 5$ G	3.83	2.5
$B_0 = B_{1,2} \pm 10$ G	5.53	0
$B_0 = B_{1,2} \pm 15$ G	5.58	0

with a very low angular scatter at $T = 297$ K. The data obtained are necessary for a deep understanding of peculiarities of the electronic structure of the spin probe and will be used for studying the influence of local distortions of the structure of the initial matrix when doping HAp by diverse cations.

FUNDING

This work was supported by the Russian Foundation for Basic Research, project no. 18-29-11086 and by the research grant of Kazan Federal University.

CONFLICT OF INTEREST

The authors declare that they have no conflicts of interest.

REFERENCES

1. Habraken, W., Habibovic, P., Epple, M., et al., *Mater. Today*, 2016, vol. 19, no. 2, p. 69.
2. Insley, G. and Suzuki, O., *Octacalcium Phosphate Biomaterials: Understanding of Bioactive Properties and Application*, Cambridge: Woodhead, 2019.
3. Safronova, T.V. and Putlyaev, V.I., *Nanosistemy: Fizika, Khimiya, Matematika*, 2013, vol. 4, no. 1, p. 24.
4. Bazin, D. and Daudon, M., *J. Spectr. Imaging*, 2019, vol. 8, p. a16.
5. Gilinskaya, L.G., Grigorieva T.N., Okuneva G.N., et al., *J. Struct. Chem.*, 2003, vol. 44, no. 4, p. 622.
6. Gilinskaya, L.G., Okuneva, G.N., and Vlasov, Y.A. *J. Struct. Chem.*, 2003, vol. 44, no. 5, p. 813.
7. Gilinskaya, L.G., Rudina, N.A., Okuneva, G.N., et al., *J. Struct. Chem.*, 2003, vol. 44, no. 6, p. 1038.
8. Golovanova, O.A. and Kutuzova, Yu.A., *Vest. Omskogo Univ.*, 2016, vol. 1, no. 79, p. 56.
9. Gabbasov, B., Gafurov, M., Starshova, A., et al., *J. Magn. Magn. Mater.*, 2019, vol. 470, p. 109.
10. Hui, J. and Wang, X., *Inorg. Chem. Front.*, 2014, vol. 1, no. 3, p. 215.
11. Barinov, S.M., *Russ. Chem. Rev.*, 2010, vol. 79, no. 1, p. 13.
12. Islam, M., Mishra, P.C., and Patel, R., *J. Environ. Manage.*, 2010, vol. 91, no. 9, p. 1883.
13. Rivera-Munoz, E.M., in *Biomedical Engineering—Frontiers and Challenges*, Fazel, R., Ed., Rijeka: InTech, 2011, p. 75.
14. Chu, S.H., Feng, D.F., Ma, Y.B., et al., *Int. J. Nanomed.*, 2012, vol. 7, p. 3659.
15. Iafisco, M., Delgado-Lopez, J.M., Varoni, E.M., et al., *Small*, 2013, vol. 9, no. 22, p. 3834.
16. Fattibene, P. and Callens, F., *Appl. Radiat. Isot.*, 2010, vol. 68, no. 1, p. 2033.
17. Shurtakova, D., Yavkin, B., Gafurov, M., et al., *Magn. Reson. Solids*, 2019, vol. 21, no. 1, art. no. 19105.
18. Abdul'yanov, V.A., Galiullina, L.F., Galyavich A.S., et al., *JETP Lett.*, 2008, vol. 88, no. 1, p. 69.
19. Chelyshev, Y., Gafurov, M., Ignatyev, I., et al., *Biomed. Res. Int.*, 2016, vol. 2016, no. 3706280, p. 1.
20. Biktagirov, T., Gafurov, M., Mamin, G., et al., *J. Phys. Chem. A*, 2014, vol. 118, no. 8, p. 1519.
21. Lysak, V.V. *Mikrobiologiya. Uchebnoe posobie* (Microbiology. Study Guide), Minsk: BGU, 2007, p. 430.
22. Buchachenko, A.L. and Vasserman, A.M., *Stabil'nye radikaly. Elektronnoe stroenie, reaktsionnaya sposobnost' i primenenie* (Stable Radicals. Electronic Structure, Reactivity, and Applications), Moscow: Khimiya, 1973, p. 408.
23. Usachev, K.S., Klochkova, E.A., Golubev, A.A., et al., *SN Appl. Sci.*, 2019, vol. 1, no. 5, p. 442.
24. Qin, P.Z. and Warncke, K., *Methods in Enzymology*, Netherlands: Elsevier, 2015, vol. 563, p. 702.
25. Qin, P.Z. and Warncke, K., *Methods in Enzymology*, Netherlands: Elsevier, 2015, vol. 564, pt B, p. 634.
26. Schiemann, O. and Prisner, T.F., *Q. Rev. Biophys.*, 2007, vol. 40, no. 1, p. 1.
27. Dzuba, S.A., *Russ. Chem. Rev.*, 2007, vol. 76, no. 8, p. 699.
28. Panesar, N., *Nat. Rev. Drug Discov.*, 2008, vol. 7, no. 8, p. 710.
29. Khambata, R.S., Ghosh, S.M., Rathod, K.S., et al., *Proc. Natl. Acad. Sci. USA*, 2017, vol. 114, no. 4, p. E550.
30. Wayne, R.P., Barnes, I., Biggs, P., et al., *Atmos. Environ. Pt A. General Topics*, 1991, vol. 25, no. 1, p. 1.
31. Stanton, J.F., *J. Chem. Phys.*, 2007, vol. 126, no. 13, p. 134309.
32. Denysenkov, V., Prandolini, M.J., Gafurov, M., et al., *Phys. Chem. Chem. Phys.*, 2010, vol. 12, no. 22, p. 5786.
33. Gizatullin, B., Gafurov, M., Vakhin, A., et al., *Energy Fuels*, 2019, vol. 33, no. 11, p. 10923.
34. Osipov, V.Y., Shames, A.I., Efimov, N.N., et al., *Phys. Solid State*, 2018, vol. 60, no. 4, p. 723.
35. Osipov, V.Y., Shakhov, F.M., Efimov, N.N., et al., *Phys. Solid State*, 2017, vol. 59, no. 6, p. 1146.
36. Gafurov, M., Biktagirov, T., Mamin, G., et al., *Phys. Chem. Chem. Phys.*, 2015, vol. 17, no. 31, p. 20331.
37. Rau, J.V., Fadeeva, I.V., Fomin, A.S., et al., *ACS Biomater. Sci. Eng.*, 2019, vol. 5, no. 12, p. 6632.
38. Yavkin, B.V., Mamin, G.V., Orlinskii, S.B., et al., *Phys. Chem. Chem. Phys.*, 2012, vol. 14, no. 7, p. 2246.

39. Goldberg, M., Gafurov, M., Makshakova, O., et al., *J. Phys. Chem. B*, 2019, vol. 123, no. 43, p. 9143.
40. Gafurov, M., Biktagirov, T., Mamin, G., et al., *Appl. Magn. Reson.*, 2014, vol. 45, no. 11, p. 1189.
41. Cox, N., Nalepa, A., Lubitz, W., et al., *J. Magn. Reson.*, 2017, vol. 280, p. 63.
42. Aliabadi, A., Zaripov, R., Salikhov, K., et al., *J. Phys. Chem. B*, 2015, vol. 119, no. 43, p. 13762.
43. Kulik, L.V., *Doctoral (Physics and Mathematics) Dissertation*, Novosibirsk: Institute of Chemical Kinetics and Combustion, Siberian Branch, Russian Academy of Sciences, 2011.
44. Schweiger, A. and Jeschke, G., *Principles of Pulse Electron Paramagnetic Resonance*, Oxford: Oxford Univ., 2001.
45. Stoll, S. and Schweiger, A., *J. Magn. Reson.*, 2006, vol. 178, no. 1, p. 42.
46. Goldfarb, D., *Emagres*, 2007, vol. 6, no. 1, p. 101.
47. Wili, N., Richert, S., Limburg, B., et al., *Phys. Chem. Chem. Phys.*, 2019, vol. 21, no. 22, p. 11676.
48. Florent, M., Kaminker, I., Nagarajan, V., et al., *J. Magn. Reson.*, 2011, vol. 210, no. 2, p. 192.
49. Jeschke, G. and Spiess, H.W., *Chem. Phys. Lett.*, 1998, vol. 293, nos. 1–2, p. 9.
50. Gracheva, I.N., Gafurov, M.R., Mamin, G.V., et al., *Magn. Reson. Solids*, 2016, vol. 18, no. 1, article no. 16102.

Translated by E. Yablonskaya